

See discussions, stats, and author profiles for this publication at: <https://www.researchgate.net/publication/263938887>

# Tailored Reactivity of Ni+Al Nanocomposites: Microstructural Correlations

ARTICLE in THE JOURNAL OF PHYSICAL CHEMISTRY C · SEPTEMBER 2012

Impact Factor: 4.77 · DOI: 10.1021/jp303407e

CITATIONS

27

READS

57

8 AUTHORS, INCLUDING:



**Khachatur V. Manukyan**

University of Notre Dame

61 PUBLICATIONS 257 CITATIONS

SEE PROFILE



**Benjamin Aaron Mason**

Schlumberger Limited

15 PUBLICATIONS 75 CITATIONS

SEE PROFILE



**Steven Son**

Purdue University

246 PUBLICATIONS 2,804 CITATIONS

SEE PROFILE



**A. S. Mukasyan**

University of Notre Dame

188 PUBLICATIONS 2,982 CITATIONS

SEE PROFILE

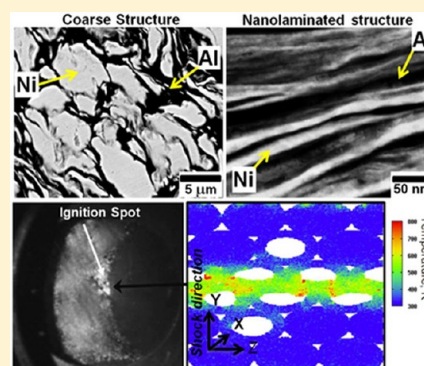
# Tailored Reactivity of Ni+Al Nanocomposites: Microstructural Correlations

Khachatur V. Manukyan,<sup>\*,†</sup> B. Aaron Mason,<sup>‡</sup> Lori J. Groven,<sup>‡</sup> Ya-Cheng Lin,<sup>†</sup> Mathew Cherukara,<sup>§</sup> Steven F. Son,<sup>‡</sup> Alejandro Strachan,<sup>§</sup> and Alexander S. Mukasyan<sup>†</sup>

<sup>†</sup>Department of Chemical and Biomolecular Engineering, University of Notre Dame, Notre Dame, Indiana 46556, United States

<sup>‡</sup>School of Mechanical Engineering and <sup>§</sup>School of Materials Engineering, Purdue University, West Lafayette, Indiana 47907, United States

**ABSTRACT:** An efficient approach that combines short-term (minutes) high-energy dry ball milling and wet grinding to tailor the nano- and microstructure of Ni+Al composite reactive particles is reported. Varying the ball-milling conditions allows control of the volume fraction of two distinct milling-induced microstructures, that is, coarse and nanolaminated. It is found that increasing the fraction of nanolaminated structure present in the composite particles leads to a decrease in their ignition temperature ( $T_{ig}$ ) from 700 and 500 K. Material with nanolaminated microstructure is also found to be more sensitive to impact ignition when compared with particles with a coarse microstructure. It is shown that kinetic energy ( $W_{cr}$ ) thresholds for impact ignition, obtained for an optimized nanolaminated microstructure, is only 100 J. High-speed imaging showed that the impact-induced ignition occurs through formation of hot spots caused by impact. Molecular dynamic simulations of a model system suggest that impact-induced localized plastic deformation raises the local temperatures to  $\sim 600$  K, enough to initiate exothermic reactions. Analysis of the kinetics and reaction mechanism shows that the reason for low  $T_{ig}$  and  $W_{cr}$  for nanolaminated microstructure is the rapid solid-state dissolution of nickel in aluminum lattices.



## 1. INTRODUCTION

Gasless (or low gas) high-energy density materials hold great promise for many applications, including chemical energy storage, microscale energetic devices, heat sources for joining of refractory substances, and synthesis of advanced materials.<sup>1–8</sup> This class of energetic materials can exhibit extraordinary properties such as fast burning rates and high combustion temperatures, accompanied by low volume expansion or even densification due to the lack of gaseous products. Aluminum-based metal–metal reactive systems are of particular interest due to their highly exothermic nature associated with intermetallic formation.<sup>9,10</sup> The combination of their mechanical properties and the ability to undergo rapid combustion reaction has prompted extensive studies aimed at investigating their use for design of structural energetic materials. One promising candidate for such applications is engineered reactive mixtures of nickel (Ni) and aluminum (Al).<sup>10–15</sup>

The exothermic reaction in the Ni+Al system may be initiated by a heat source<sup>14–16</sup> or mechanical impact.<sup>1,17–19</sup> In the first case, the ignition temperature is often considered to be a primary indicator of reaction sensitivity. The behavior of exothermic systems during external heating can be described by thermal explosion (or volumetric self-ignition) theory developed for gas-phase reactions<sup>20–22</sup> and also adapted to the homogeneous condensed systems.<sup>23</sup> These classical theories introduce several terms and conditions. For example, the difference between bulk thermal explosion and local ignition

phenomena needs to be delineated. Thermal explosion occurs when the thermal relaxation time of the reactive media is much smaller than the chemical reaction time. As a result, the entire sample ignites simultaneously. Otherwise, the reaction can be initiated locally; that is, the reaction begins at discrete locations within the sample that meet the ignition criteria. The reaction may then self-propagate throughout the sample in the form of a combustion wave with a defined speed.<sup>24</sup>

Most experimental studies have shown that the self-ignition temperature of micrometer-scale Ni+Al mixtures is equal to or above the eutectic temperature of the system ( $\sim 912$  K).<sup>3,4,25,26</sup> Therefore, the ignition phenomenon of the micrometer-scale mixtures is correlated to the formation of a liquid phase. Early experimental studies show that nickel rapidly dissolves into aluminum melt, and aluminum-rich  $Al_3Ni$  and  $Al_3Ni_2$  intermediate phases were observed in quenched samples in the initial stage of the process.<sup>26</sup> Before reaching the maximum reaction temperature (1911 K), the precipitation of solid AlNi phase from the supersaturated solution and the melting of the remaining solid nickel take place.<sup>3,26</sup> Atomistic simulations also demonstrate the importance of Al melting in thermal and dynamically initiated composites.<sup>27–29</sup>

Received: April 10, 2012

Revised: July 11, 2012

Published: September 5, 2012

In the case of mechanically induced reaction, the impact energy or projectile velocity may be used as a measure for the chemical reaction sensitivity. However, little is known about the effect of constituent properties on the threshold condition for reaction ignition. It was shown that for microscaled Ni+Al mixtures the threshold of impact velocities above which reaction may occur are greater than 1000 m/s ( $\sim 10$  kJ).<sup>19</sup> However, for successful design of structural energetic materials the threshold of impact velocities (energies) of Ni+Al mixtures must be decreased significantly.

Recently, it was demonstrated that high-energy ball milling could enhance the reactivity and ignition sensitivity of the Ni+Al system.<sup>1,9,13,14,17</sup> Such mechanical treatment significantly decreases both the ignition temperature (down to 600 K),<sup>14</sup> as well as diminishes the value of critical impact energies ( $W_{cr}$ ) required to initiate the reaction to 420 J.<sup>17</sup> High-energy ball milling is a complex process that involves intensive interaction between the particles and milling media.<sup>30</sup> It was shown that for mixtures with ductile compounds (e.g., Ni+Al powder mixture) flattening and cold welding of metal particles occurs in the initial stage of DM.<sup>30–32</sup> An increase in composite particle sizes may also be observed in this stage. Longer processing causes strength hardening of the material. Consequently, its brittleness may increase, resulting in fragmentation of the composite particles. Further milling may lead to the formation of solid solutions, intermetallic, or amorphous phases or even cause sudden initiation of the exothermic reaction.<sup>33</sup> However, the influence of microstructural transformations on thermal and mechanical sensitivity of formed composite particles has not yet been fully investigated. Other open questions are how solid-state mass transfer alone can be responsible for the self-sustained reactions ignition in such systems and why they can be ignited by surprisingly low-impact energies.

This work is a continuation of our efforts to more fully answer some fundamental issues with regards to the role of ball-milling-induced microstructure for the thermal and mechanical impact in the Ni+Al system. First, the influence of the sequence and duration of applied milling/grinding steps on the microstructure of the produced composite particles was investigated. Second, the correlations between particles microstructures on both thermal and mechanical sensitivities of the reactive systems were revealed. Third, the kinetics and reaction mechanism for reactive medium with selected microstructures were experimentally explored. Fourth, the atomistic simulation of ignition processes was used to define the possible mechanism for the impact-induced reaction initiation. Finally, based on all of the above results, the nature of the relationship between thermal and mechanical initiation characteristics was established.

## 2. EXPERIMENTAL AND THEORETICAL METHODS

**2.1. Materials Fabrication.** Aluminum (Alfa Aesar, particle size  $<45\ \mu\text{m}$ ) and nickel (Alfa Aesar, particle size  $\sim 5\ \mu\text{m}$ ) powders were used as initial reactants. Two-step high-energy ball milling of an equiatomic Ni+Al mixture in 99.9998% pure argon atmosphere was performed by using PM100 (Retsch, Germany) planetary ball mill within 250 mL stainless steel jar. Stainless-steel balls with diameter 10 mm were used as milling media. The ball-to-mixture ratio was 5:1. The rotational speed was 650 rpm. First, 35 g batches of the reactant powders were subjected to dry milling (DM) for different time durations. The time duration was selected as  $\sim 25$ , 50, 75, and 97% of critical milling time ( $t_{crit} = 17.5$  min) when exothermic reaction occurs

during milling. Each batch was milled in one to four intervals consisting of up to 5 min of milling, followed by a 15 min rest to prevent excessive heating of the material during milling. Because a process control agent was not present in this stage, resulting particles were relatively large in size, having diameters up to 3 mm. After DM, the cooled jar was opened and 20 mL of hexane (98.5% hexane isomers, Mallinckrodt Chemicals) was added. Subsequent wet grinding (WG) in hexane was performed for a total of 10 min (two intervals of 5 min of milling, followed by a 15 min rest) with the same milling conditions, except that the jar was pressurized with argon to  $\sim 0.3$  MPa. One batch of the Ni+Al mixture was wet ground without preliminary DM for comparison. After such treatment, the samples were dried in air for 1 h and then vacuum-dried at  $\sim 300$  K, for 1 h to remove the hexane fully. As-milled powders were sieved into six fractions ( $F_i$ ) with the following ranges of particle sizes ( $d$ ):  $d < 25\ \mu\text{m}$  ( $F_1$ );  $25\text{--}53\ \mu\text{m}$  ( $F_2$ );  $53\text{--}106\ \mu\text{m}$  ( $F_3$ );  $106\text{--}355\ \mu\text{m}$  ( $F_4$ );  $355\text{--}850\ \mu\text{m}$  ( $F_5$ ); and  $d > 850\ \mu\text{m}$  ( $F_6$ ).

**2.2. Reaction Initiation.** The ignition temperature of the materials produced with high-energy ball milling was measured using a simple setup (Figure 1a) that includes a hot plate, a

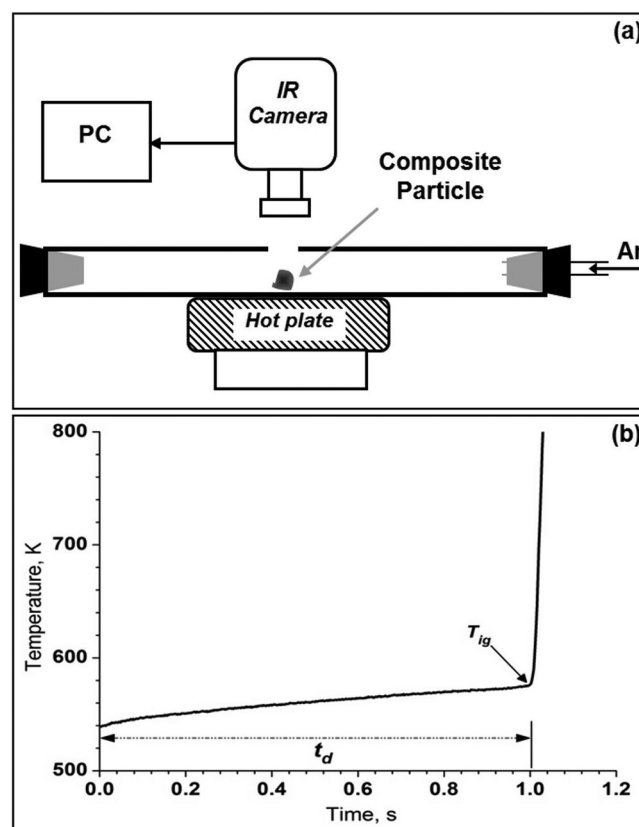


**Figure 1.** Experimental setup (a) for measuring temperature–time history (b) of a Ni+Al composite particle.

quartz tube (300 mm in length, 15 mm inner diameter, and 1 mm wall thickness) with a small opening (5 mm  $\times$  5 mm) in the middle, and high-speed infrared (IR) camera (FLIR Systems, SC6000). The latter allowed measurement (spatial resolution of  $2\ \mu\text{m}$ , temperature resolution of 5 K, and recording speed of 1000 frame/s) of the temperature–time history of the process (Figure 1b) and thus defines the ignition temperature ( $T_{ig}$ ) of the composite particles. In the typical

thermal initiation experiment the quartz tube was placed on the hot plate and heated to 700 K, which remains constant during the experiments. Pure argon (99.9998%) was purged (50 cc/min) through the tube for 10 min to eliminate air. Then, a selected composite particle was placed into the tube through the opening. In such a way classical conditions are arranged for measuring the ignition characteristics, with the reacting system (composite particle) being immersed into the furnace maintained at a constant temperature. The sizes of Ni+Al composite particles were relatively small (10–1000  $\mu\text{m}$ ) with heat relaxation times ( $\tau \approx d^2/\alpha$  and assuming  $\alpha \approx 10^{-1} \text{ cm}^2/\text{s}$  for the thermal conductivity of the particle) in the range from  $10^{-6}$  to  $10^{-2}$  s, which is well below typical ignition delay times ( $t_d \approx 1\text{--}10$  s). This means that the entire particle is uniformly heated during the experiments. The temperature–time history of the surface of the particle was measured by an IR camera positioned just above the opening. A typical temperature profile is shown in Figure 1b. It can be seen that at a particular temperature a dramatic change in the slope of the curve takes place. The corresponding temperature is considered to be the ignition temperature ( $T_{\text{ig}}$ ) of the composite particle. The average values for  $T_{\text{ig}}$  were calculated based on data of at least five ignition experiments of the same material.

Reaction initiation by mechanical impact was performed through a combined compression/shear experiment used previously with explosives.<sup>34</sup> The schematic of the experiments is shown in Figure 2. For these experiments, the ball-milled

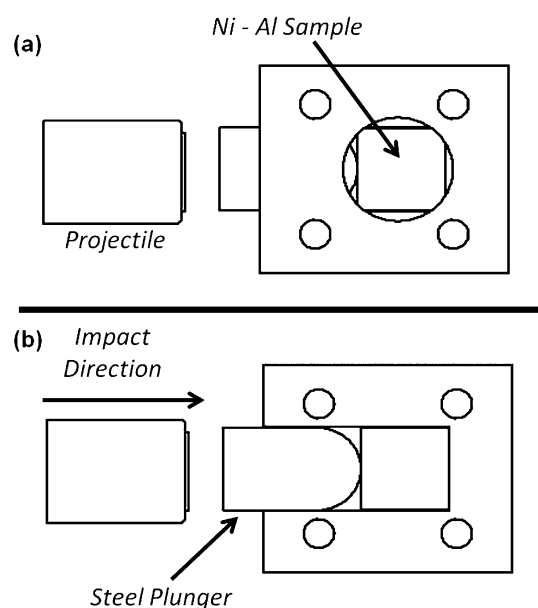


**Figure 2.** Scheme of compression/shear tests: windowed sample holder with sample (a) and plunger and projectile (b).

materials were compacted into square samples with nominal dimensions of 20 mm  $\times$  20 mm  $\times$  2 mm by applying a uniaxial pressure of 670 MPa. The initial samples' relative density was in the range of 68–72% TMD. Compacted samples were placed into a specially designed holder equipped with an acrylic window (Figure 2). A steel flyer plate press fitted into a projectile (24 g in total mass) is accelerated by means of a gas gun, travels toward the sample, and impacts a plunger inserted in a slot on the side of the holder. Plungers of 2 mm thickness and impact face having a 10 mm radius were used in the experiments. The gas gun used in these experiments propels a

25.4 mm diameter projectile at velocities up to 1000 m/s. The impact is monitored by a high-speed camera (Vision Research; Phantom v7.3; Wayne, NJ) at frame rates up to 88 000 frames per second.

**2.3. Materials Characterization.** Materials before and after reaction were examined by field-emission scanning electron microscopy (LEO series EVO 50) equipped with an Oxford Instrument EDS analyzer. Scanning transmission electron microscope (STEM) images of ball-milled materials were also taken by a Magellan 400 (FEI) field-emission scanning electron microscope (SEM). Samples for STEM analysis were prepared by using a Helios NanoLab600 system (FEI). The phase compositions of materials were determined by X-ray diffraction (XRD) analysis with Ni-filtered Cu  $K\alpha$  radiation (D8 Advance, Bruker and Scintag, X1 Advanced Diffraction System, Scintag) operated at 40 kV and 40 mA. Step-scan data (of step size 0.025° and counting time up to 15 s) of ball-milled materials were recorded for the angular range 20–80° ( $2\theta$ ).

The heat of reaction and kinetics of heat release for different ball-milled samples were measured in a TA Instruments Q600 simultaneous thermogravimetric analyzer and differential scanning calorimeter (TGA/DSC). In each scan,  $\sim 20$  mg of reactive material was heated to 1070 K at different heating rates (10, 20, and 50 K/min) in an atmosphere of 99.9998% pure argon with flow rate 100 cc/min. Apparent activation energies for all investigated systems were estimated according to the Kissinger method.<sup>35</sup>

#### 2.4. Nonequilibrium Molecular Dynamics Simulations.

Molecular dynamics (MD) simulations of a model nanostructure were used to explore possible mechanisms of shock-induced chemical initiation operating in the ball-milled samples. While providing a very detailed description of dynamical loading and subsequent reactions, MD simulations are computationally intensive and thus limited to relatively small sizes (tens to hundreds of nanometers on a side) and short time scales (nanoseconds). Thus we study shock loading and subsequent reactions for a simplified model of nanostructure over a relatively short time period. To capture the porosity of the ball-milled samples, we consider an atomistic model containing 18 particles of cylindrical shape with 12 nm radius and 8.8 nm in height (Figure 3). Periodic boundary conditions are applied in all three directions leading to a columnar nanostructure with  $\sim 4$  million atoms in the simulation cell of dimensions 8.8 nm along  $x$ , 131 nm along  $y$  (the shock direction), and 72.9 nm along  $z$  including a 5 nm gap in the center of the cell where impact will occur. The cylindrical particles have an internal lamellar nanostructure consisting of alternating Ni and Al layers, with a period of  $\sim 7$  nm with (111) interfaces. The particles are randomly oriented around their axis and arranged in a closed-packed structure. To reach the 72% TMD of the experimental samples, we carved out cylindrical voids inside each particle. Voids with radius 5.45 nm reduce the TMD  $\sim 90\%$  of the original full cylinder system to  $\sim 72\%$  to match the experiment free-volume fraction. We stress that the model nanostructures differ significantly from those of the samples prepared via high-energy ball milling; despite these limitations, the simulation sheds light onto mechanisms that can contribute to the initial chemistry and energy localization in the experimental samples.

The LAMMPS<sup>36,37</sup> simulation package was used to perform the atomistic simulations with an embedded atom potential developed by Purja and Mishin<sup>38</sup> to describe the atomic



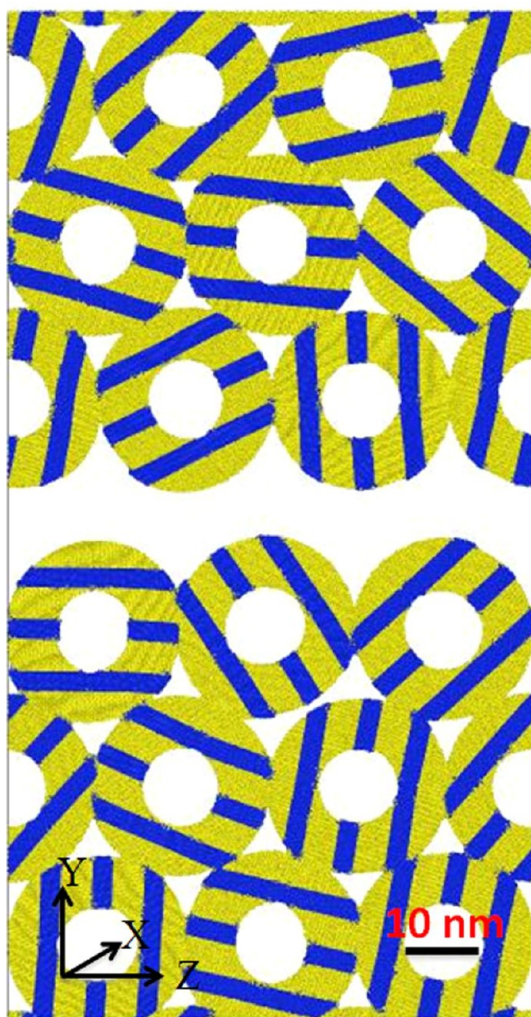


**Figure 3.** Initial structure for the nonequilibrium MD simulation of dynamical loading of porous Ni+Al samples.

interactions. The sample was thermalized over multiple stages to obtain the final equilibrated structure. We start with a bulk Ni/Al laminate of period 6.62 nm built from unit cells oriented along  $[11\bar{2}]$ ,  $[1\bar{1}0]$ , and  $[111]$ . To minimize lattice mismatch, we replicated the Ni unit cell 20 times along  $[11\bar{2}]$  and 35 times along  $[1\bar{1}0]$ , whereas the Al unit cell was replicated 17 and 30 times, respectively. This structure is then thermalized for 50 ps at 300 K and 1 atm using constant temperature and stress MD (NPT ensemble). Hollow cylinders are then carved out of this bulk laminate. After energy minimization of these structures, a two-stage thermalization is performed: 30 K for 200 ps at constant stress, constant temperature, followed by for 1270 ps at 300 K. The entire sample was then assembled as described above, and a further thermalization under constant stress and temperature was performed at 300 K for 375 ps. We generate shockwaves by driving the two halves of the composite samples into one another at the desired particle velocity. This is accompanied by moving the periodic simulation cell length in the shock direction<sup>39–41,45</sup> to enable the description of nonequilibrium shock loading and as well as the subsequent evolution of the system including chemical reactions under isenthalpy or energy conditions. The atoms in the top half are given a velocity of  $(-u_p)$  in addition to their thermal velocity in the  $y$  direction, whereas those in the bottom half are given a

velocity of  $(u_p)$ . To maintain velocity continuity across the periodic boundary in the  $y$  direction, the upper boundary moves down at  $(-u_p)$  while the lower one moves up at  $(u_p)$ . After impact, two shock waves propagate away from the central region and eventually meet at the cell boundary. At this point, just as the two shock waves have passed through the system, the shrinking boundary is stopped and a constant volume, constant energy (NVE) run is started. This allows us to study the shock-induced chemistry in the shocked composite at time scales significantly longer than those of the dynamical loading.

To characterize the local chemistry in the sample over the course of the simulation, we define an atomic-based local reaction coordinate. The simulation domain is divided into a 2-D square mesh in the  $y$ - $z$  plane, each cell being  $0.5 \text{ nm} \times 0.5 \text{ nm}$ . The local reaction coordinate ( $\eta$ ) is computed for each cell from the number of Ni and Al atoms in its volume ( $N_{\text{Ni}}$  and  $N_{\text{Al}}$ )

$$\chi = N_{\text{Ni}} / (N_{\text{Ni}} + N_{\text{Al}})$$

$$\eta = \frac{100}{45} * \chi N_{\text{Ni}} \quad \text{if } 0 \leq \chi N_{\text{Ni}} \leq .45$$

$$\eta = \frac{100}{45} * (1 - \chi N_{\text{Ni}}) \quad \text{if } .55 \leq \chi N_{\text{Ni}} \leq 1$$

$$\eta = 1 \quad \text{if } .45 < \chi N_{\text{Ni}} < .55$$

This reaction coordinate varies linearly from 0 for a cell containing only Ni or only Al atoms to 1 for a cell containing 50% of each. An overall reaction coordinate for the entire system is obtained by averaging over cells weighted by the number of atoms. This parameter is used to follow the overall chemistry in the system over the course of the shock loading and subsequent reactions.

### 3. RESULTS

**3.1. Characterization of Reactive Ni–Al Composite Materials.** To evaluate the milling induced microstructural evolution, we first imaged the initial reactant mixture, showing that it consists of irregular Al particles with sizes of 15–30  $\mu\text{m}$  and spherical shaped fine ( $\sim 5 \mu\text{m}$ ) Ni particles (Figure 4a). SEM investigation suggests that within the early stage of DM the initial particles of Ni and Al deform into lamella type structure and cold welding process starts. At  $t_{\text{DM}} = 4 \text{ min}$ , large (up to 3000  $\mu\text{m}$ ) Ni+Al composite particles are already formed, as shown in Figure 4b. These composite particles have relatively uniform microstructure with characteristic scale of heterogeneity of several micrometers, below referred as “coarse” microstructure. With increasing  $t_{\text{DM}}$ , a new much finer microstructure starts to form on the surface of the composite particles (Figure 4c). The thickness of the layers is in the range of 150–200  $\mu\text{m}$ .

Close inspection of the composite particles (Figure 5a,b) obtained at  $t_{\text{DM}} = 17 \text{ min}$  shows that the core still contains relatively large slightly deformed Ni grains (bright contrast) surrounded by the Al matrix (dark area). However, high-magnification SEM (Figure 5c) of the surface layer shows that the Ni and Al in such area are mixed much more uniformly. Scanning TEM image of the surface layer (Figure 5d) indicates that Ni and Al are mixed homogeneously, forming a fine “nanolaminated” structure. The thickness of each metal layer in this structure is  $\sim 20$ –30 nm. Statistical analysis of such images showed that DM forms large (500–3000  $\mu\text{m}$ ) composite particles with a coarse core structure and surface layers (100–

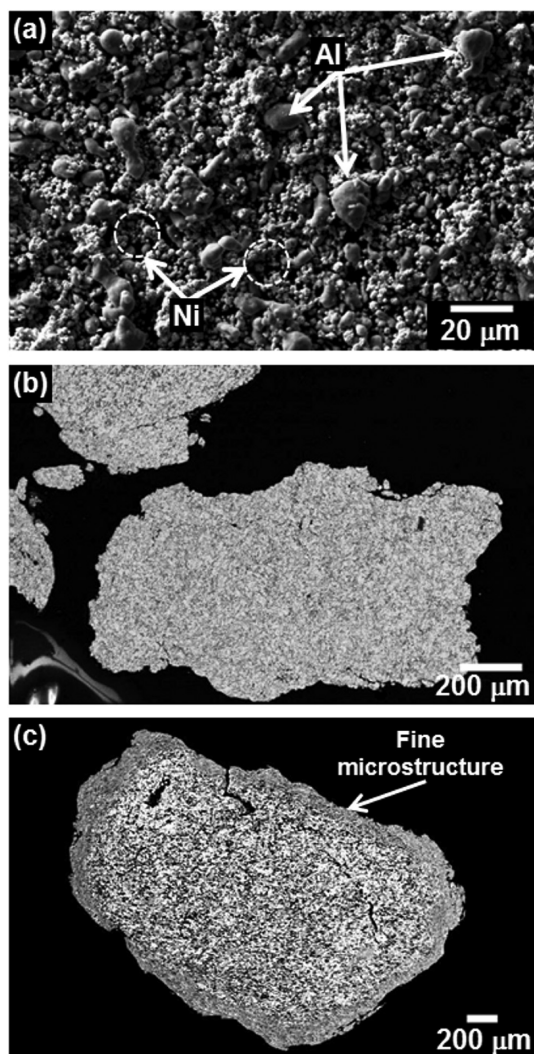


**Figure 4.** SEM images of initial Ni+Al mixture (a) and composite particles obtained after 4 (b) and 17 (c) min of dry ball milling.

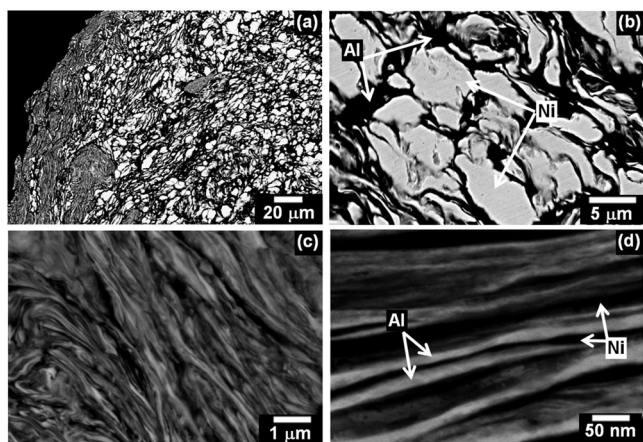


**Figure 5.** High-magnification images for material obtained at 17 min of ball milling (a), coarse (b), and nanolaminated microstructures (c,d).

250 μm thick) of nanolaminated microstructure. Some small amount (<10% of total particles) of fine particles ( $d \approx 150$ –250 μm) with solely fine microstructure was also observed.

Therefore, to control the particles' microstructure, that is, the ratio between coarse and nanolaminated structures, we

conducted a series of experiments with a varied combination of DM and WG. This allowed further fracturing and refining of the large (500–3000 μm) composite particles formed during DM as well as removed cold-welded material from the milling balls and the jar. The SEM investigations of as-treated powders showed that although some large composite particles could still be found in the DM+WG material, the portion of smaller particles ( $d < 500$  μm) with nanolaminated microstructure significantly increased. For further microstructural investigations, each DM+WG material was sieved, and microstructures of each fraction were studied. These investigations showed that depending on the ball-milling conditions one may produce particles with either coarse or nanolaminated microstructures or particles with a combination of both. To visualize the effect of ball milling on microstructural transformation, we analyzed SEM images by ImageJ software.<sup>42</sup> On the basis of the measurements of areas occupied by the coarse and nanolaminate structures a qualitative diagram showing the effect of milling on microstructure for the various particle size ranges was developed (Figure 6).

The first row in the diagram (Figure 6) shows that after 10 min of WG mainly coarse structure formed for most sizes, with nanolaminated structure observed only for small particles ( $F_1$  and  $F_2$  powders). Although the  $t_{DM(4 \text{ min})} + t_{WG(10 \text{ min})}$  milling conditions yield material with primarily coarse structure (row 2), nanolaminated structures are observed on the surface of the large particles ( $d > 355$  μm). Longer DM increases the portion of nanolaminated structure that was observed. For example, after  $t_{DM(8.5 \text{ min})} + t_{WG(10 \text{ min})}$ , the fine nanostructure was observed in all size ranges (row 3). However, for larger particles, the coarse microstructure is still prevalent. Further increase in DM time results in the nanolaminated structure being dominant for almost all fractions (rows 4 and 5).

Comparison of XRD patterns (Figure 7) for the initial Ni+Al mixture and  $F_2$  fractions of material obtained at  $t_{DM(4 \text{ min})} + t_{WG(10 \text{ min})}$  (only coarse microstructure) and  $t_{DM(17 \text{ min})} + t_{WG(10 \text{ min})}$  (only nanolaminated microstructure) conditions suggests that the applied ball-milling process does not lead to the formation of any intermetallic phases. It is important to note that whereas diffraction peaks are broader for the ball-milled powders, their positions are not shifted from those for the initial mixture. This indicates that metallic solid-solutions are not formed. These results were confirmed by EDS measurements of elemental compositions in Ni and Al layers showing, with accuracy of 0.1 wt %, the absence of metal dissolution.

**3.2. Reactivity of Materials. Thermal Initiation of Reaction.** Examination of the thermal ignition characteristics as a function of the distinct milling-induced microstructures showed that  $T_{ig}$  for materials obtained by solely DM (17 min), where particles with coarse structure are dominant, is  $720 \pm 25$  K. Note that this temperature is well below the eutectic in the Ni–Al system (912 K). Furthermore, it was demonstrated that varying the DM time and adding a WG step enables additional tuning of the thermal ignition temperature. Results of these experiments (Figure 8) suggest that, for example, at  $t_{DM(0 \text{ min})} + t_{WG(10 \text{ min})}$ , the  $T_{ig}$  decreases from 700 to 550 K with decreasing of particle sizes in the range 106 to 25 μm. Ignition behaviors for materials obtained at  $t_{DM(8.5 \text{ min})} + t_{WG(10 \text{ min})}$  and  $t_{DM(13 \text{ min})} + t_{WG(10 \text{ min})}$  were found to be close to each other. For these conditions,  $T_{ig}$  for  $F_1$  fractions is below 575 K. At  $t_{DM(17 \text{ min})} + t_{WG(10 \text{ min})}$ , the composite particles for all size fractions were observed to be the most thermally sensitive materials evaluated.



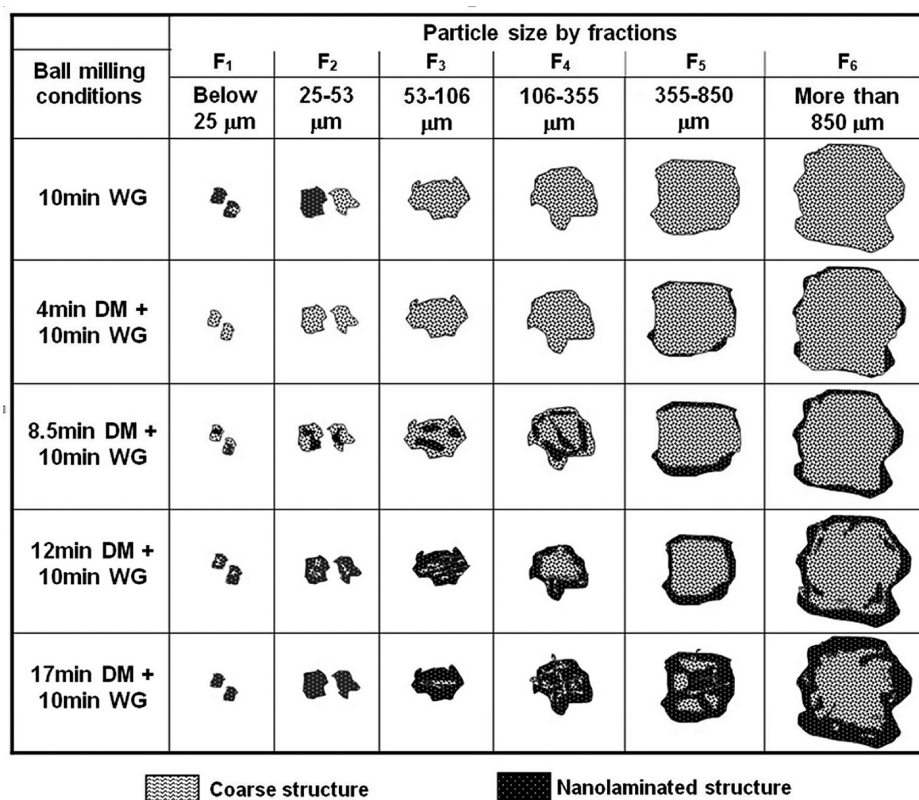


Figure 6. Diagram showing all possible combinations depending on particle size and ball-milling duration.

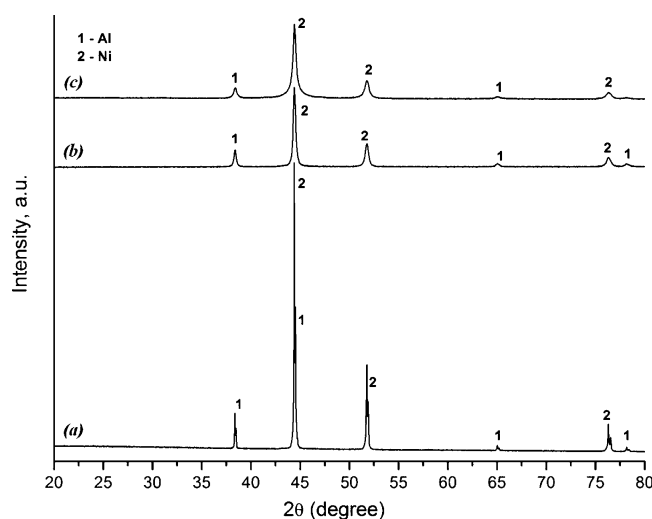


Figure 7. XRD patterns of initial mixture Ni+Al mixture (a) and materials with coarse (b) and nanolaminated (c) structures.

Most of the size fractions in this material were ignited at temperatures below 575 K. The lowest ignition temperature,  $\sim 500$  K, was observed for the smallest (F<sub>1</sub>) fraction. The analysis of the results for reaction ignition experiments (Figure 8) together with microstructural transformation diagram (Figure 6) suggests that the ignition temperature of Ni+Al composite particles with coarse microstructure is  $\sim 700$  K, whereas for fine nanolaminated structure it is as low as 500 K. The composite particles involving both observed microstructures have an ignition temperature between 500 and 720 K, which is a function of the relative quantity of each microstructure present.

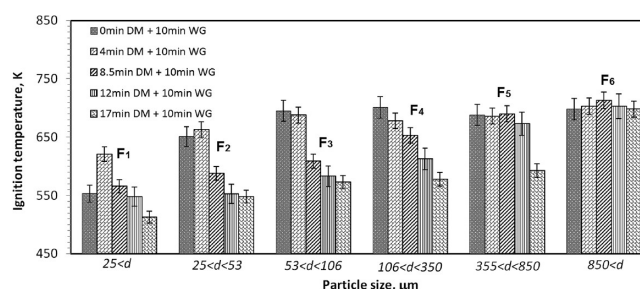
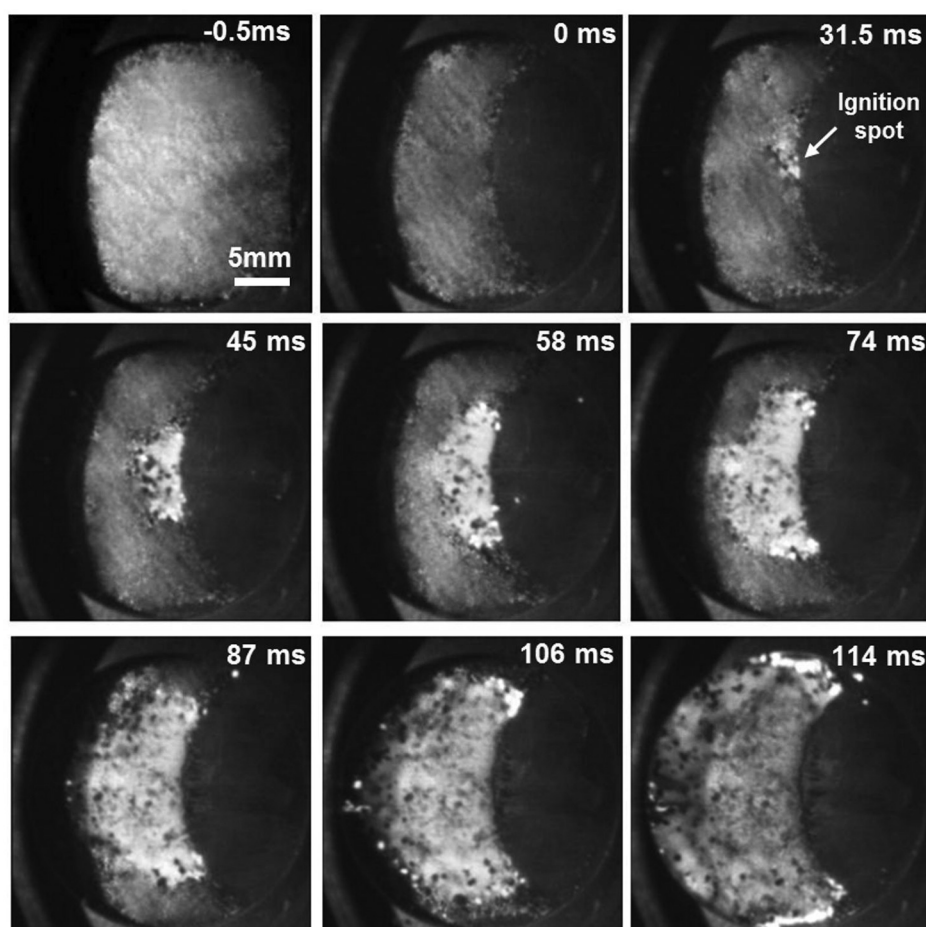


Figure 8. Ignition temperature for Ni+Al materials obtained at various milling conditions as a function of particle size.

**Reaction Initiation by Mechanical Impact.** Impact experiments under conditions described in the Experimental and Theoretical Methods section were performed to study the effect of the microstructure of ball-milled Ni+Al materials on the impact sensitivity. In the first set of experiments the impact sensitivity as a function of DM time ( $t_{\text{DM}}(X \text{ min}) + t_{\text{WG}}(10 \text{ min})$ ) was studied for F<sub>2</sub> size fraction. The results showed that for materials DM at  $X = 0$  and 4 min, reaction could not be initiated by the impact velocity produced at a projectile speed of 130 m/s (210 J). However, mixtures obtained at  $8 \leq X \leq 17$  min were consistently ignitable by this impact energy, and the initiation threshold velocity was as low as 90 m/s (kinetic energy 100 J) for mixtures obtained at  $X = 17$ . Note that samples compacted from the initial mixture of the Ni+Al powders could not be ignited with an impact velocity as high as 1000 m/s (12 kJ).

Analysis of frames (Figure 9) obtained by high-speed imaging, for example, with material produced at  $t_{\text{DM}}(17 \text{ min}) + t_{\text{WG}}(10 \text{ min})$  (F<sub>4</sub> fraction) conditions showed a delay of 32 ms between the completion of the shock deformation from the



**Figure 9.** Sequence of high-speed video images from a shear impact test for material obtained at  $t_{\text{DM}}(17 \text{ min}) + t_{\text{WG}}(10 \text{ min})$  milling conditions.

plunger and the first hot spot appearance close to the surface of the plunger. Over the following  $\sim 80$  ms, this high-temperature area expands in the form of reaction wave with propagation velocity of  $20 \pm 3$  cm/s.

To show the effect of particle size on the ignition characteristics, we performed another set of impact experiments with all six fractions of the ball-milled material under  $t_{\text{DM}}(17 \text{ min}) + t_{\text{WG}}(10 \text{ min})$  conditions. Figure 10 presents the Go/No-Go results for reactions in the impacted materials. Interestingly, the obtained data suggest that a projectile speed threshold ( $\sim 90$

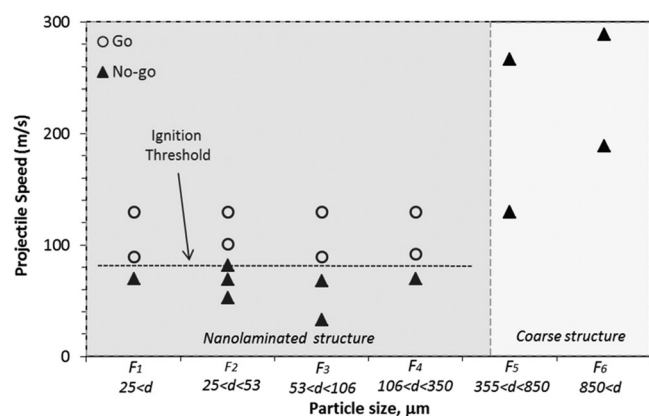


**Figure 10.** Impact ignition results for material obtained at  $t_{\text{DM}}(4 \text{ min}) + t_{\text{WG}}(10 \text{ min})$  milling conditions as a function of particle size.

m/s;  $W \approx 100$  J) to initiate the reaction does not depend on the particle sizes for sizes less than  $350 \mu\text{m}$  ( $F_1$  to  $F_4$  size fractions). Samples prepared with particles larger than  $350 \mu\text{m}$  ( $F_5$  and  $F_6$  fraction) could not be ignited even at a 300 m/s projectile speed. Figure 5 indicates that those size fractions contain a significant portion of coarse microstructure.

The XRD patterns (Figure 11a,b) reveal that AlNi is the main phase in the reacted material. Some low intensity peaks for  $\text{Al}_3\text{Ni}_2$  and  $\text{AlNi}_3$  phases were also detected. The presence of those phases is probably due to the rapid cooling of the sample after the reaction. The SEM images of samples for ball-milled material,  $t_{\text{DM}}(17 \text{ min}) + t_{\text{WG}}(10 \text{ min})$ , before (Figure 11c) and after (Figure 11d) impact initiated reaction show two main effects. First, the interparticle porosity of the sample decreases due to impact-induced plastic deformation. Second, while morphology of the particles (shape and overall size) remains essentially the same their internal porosity increases due to specific volume shrinkage during chemical reaction; the TMD of the initial composite particle is  $5.16 \text{ g/cm}^3$ , whereas the TMD of NiAl is  $5.92 \text{ g/cm}^3$ . Finally, backscattering SEM images of reacted material (Figure 11d) indicate the presence of several phases. EDS analysis suggests that gray phase corresponds to the AlNi compound, whereas lighter phase consists of  $\text{Al}_3\text{Ni}_2$  and  $\text{AlNi}_3$ .

**Kinetics and Mechanism.** As previously discussed, it was demonstrated that Ni+Al composite particles have two different microstructures, which are formed under different ball-milling conditions. These microstructures control the ignition charac-



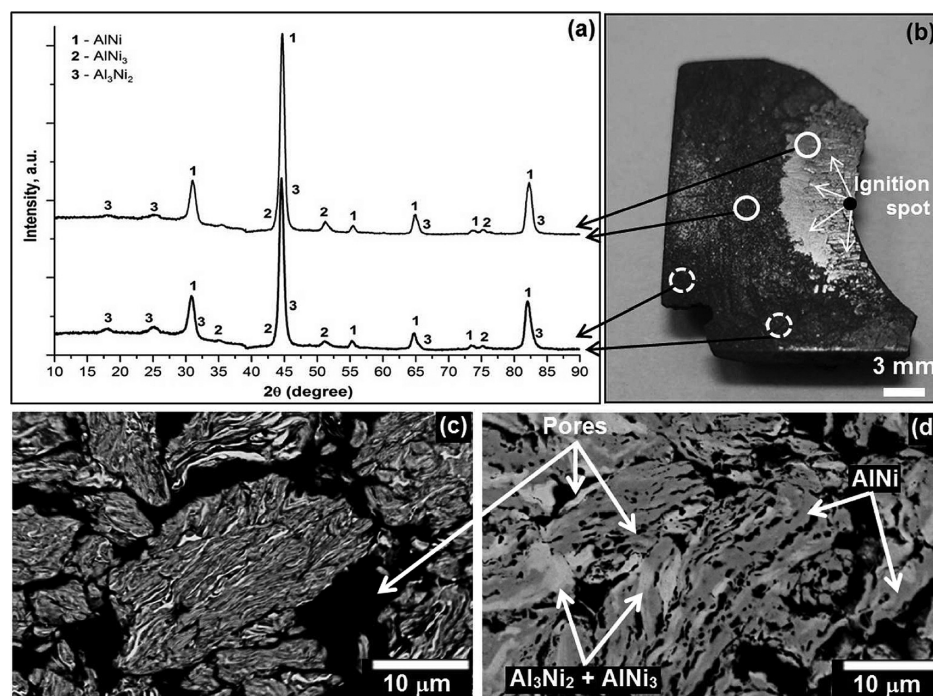


**Figure 11.** XRD patterns (a) taken from various parts of reacted sample (b) and SEM microstructure of sample before (c) and after reaction (d).

teristics of the system. In particular, material with fine nanolaminated structure can be ignited at unusually low temperatures ( $\sim 500$  K), whereas the critical temperature for initiation of reaction in particles with coarse microstructure is as high as 700 K.

To study the kinetics of chemical reactions for composite materials obtained at  $t_{DM(4\text{ min})} + t_{WG(10\text{ min})}$  (coarse) and  $t_{DM(17\text{ min})} + t_{WG(10\text{ min})}$  (nanolaminated) conditions, we conducted DSC analysis for  $F_2$  fractions (diameters between 25 and 53  $\mu\text{m}$ ) of these powders at different heating rates, as described in the Experimental and Theoretical Methods section. Typical DSC curves recorded at 20 K/min heating rate showed (Figure 12) that both materials reacted exothermically in the temperature range from 450 to 850 K, exhibiting three exothermic peaks before the melting point of aluminum (933 K). No endothermic peak was observed, indicating unreacted aluminum melting. The peaks observed for powder

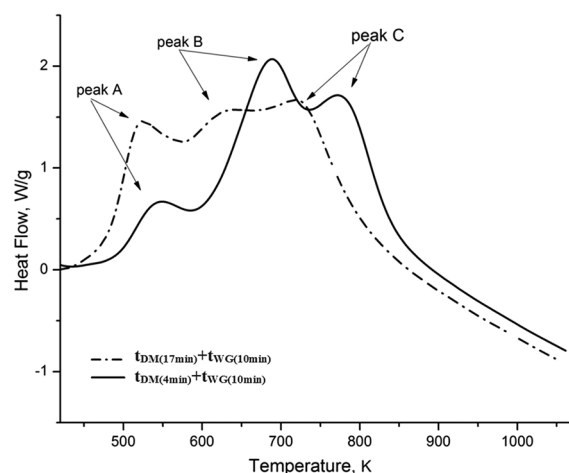


**Figure 12.** DSC curves for materials with different microstructures.

with coarse microstructure were shifted to a higher temperature range by 30–70° as compared with nanolaminate structured material. Also, for powders with nanolaminated microstructure the first, *peak A*, is more significant, whereas *peaks B* and *C* are stronger for particles with coarse microstructure. By integrating the net heat flow with respect to time, the heat of reaction was calculated to be  $104.5 \pm 2$  and  $98 \pm 3.2$  kJ/mol for materials with nanolaminated and coarse structures, respectively. Both values are only slightly smaller than the enthalpy of formation for NiAl phase from elements (118.4 kJ/mol).<sup>4</sup> From these data, one can conclude that for both materials conversion to product mainly takes place below the melting point of aluminum.

To identify the reaction mechanism, we analyzed quenched materials from DSC experiments in various stages. The XRD patterns and cross-section of quenched materials with coarse microstructure are shown in Figure 13. The XRD pattern for the material quenched at 540 K (peak A) shows peaks corresponding to nickel and aluminum. EDS analysis suggests (Figure 13b) that darker areas in the composite particle contain 90 at % Al and 10 at % Ni, whereas the brighter phase is pure Ni. This indicates that the first exothermic peak observed in DSC (peak A) corresponds to the dissolution of nickel atoms at the aluminum lattice. The material quenched at 690 K (peak B) consists of three phases: Ni,  $\text{Al}_3\text{Ni}$ , and  $\text{Al}_3\text{Ni}_2$ . Typical SEM cross sections for these particles are shown in Figure 13c. The brighter areas are nickel, whereas gray areas consist of  $\text{Al}_3\text{Ni}$  and  $\text{Al}_3\text{Ni}_2$  phases. Finally, material quenched at 770 K (peak C) contains nickel,  $\text{Al}_3\text{Ni}_2$ , and AlNi phases (Figure 13d). Although AlNi is the main phase for material quenched at 1070 K, a small amount of  $\text{AlNi}_3$  was also detected by XRD and EDS techniques (Figure 13e). Similar stepwise conversion of reagents was also observed for nanolaminated structure (Figure 14).

Finally, to calculate apparent activation energies for the various reaction steps, we conducted DSC experiments for both

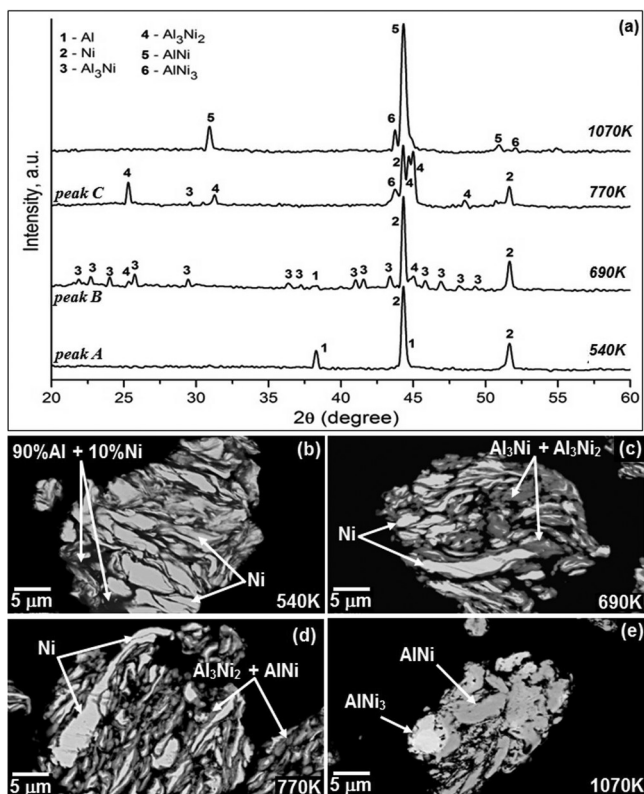


Figure 13. XRD patterns (a) and SEM images (b–e) for material obtained under  $t_{\text{DM}}(4 \text{ min}) + t_{\text{WG}}(10 \text{ min})$  conditions after annealing at different temperatures.

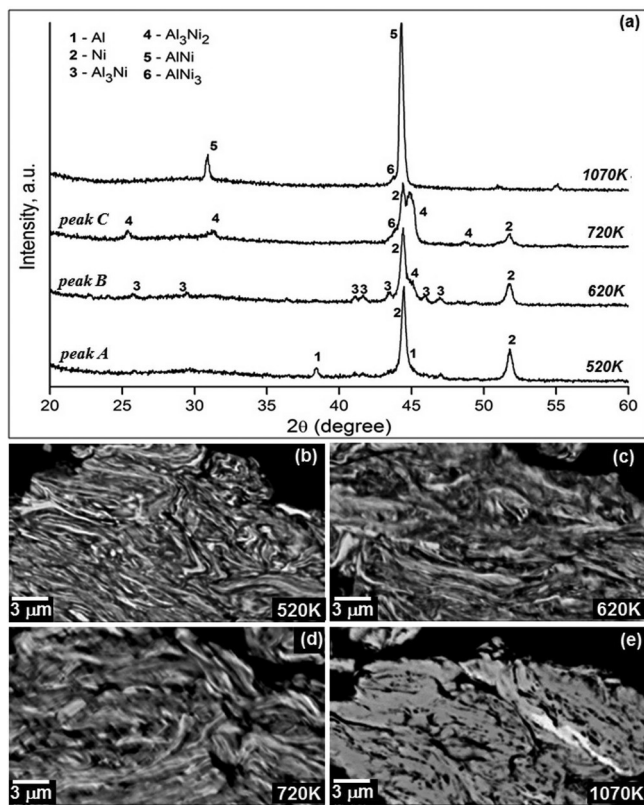


Figure 14. XRD patterns (a) and SEM images (b–e) for material obtained at  $t_{\text{DM}}(17 \text{ min}) + t_{\text{WG}}(10 \text{ min})$  conditions after annealing at different temperatures.

materials at different heating rates. Figure 15 presents the Arrhenius-type dependencies for the  $F_2$  fractions of both

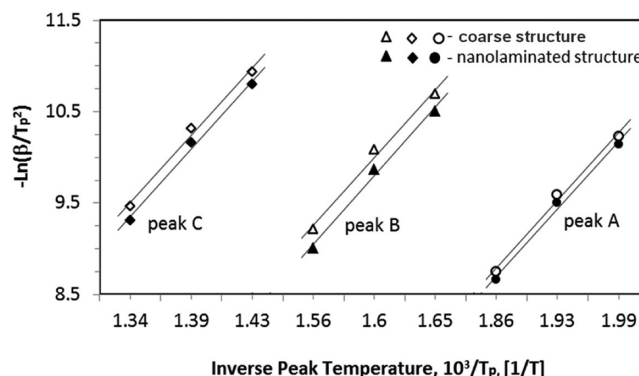


Figure 15. Kissinger analyses of chemical kinetics.

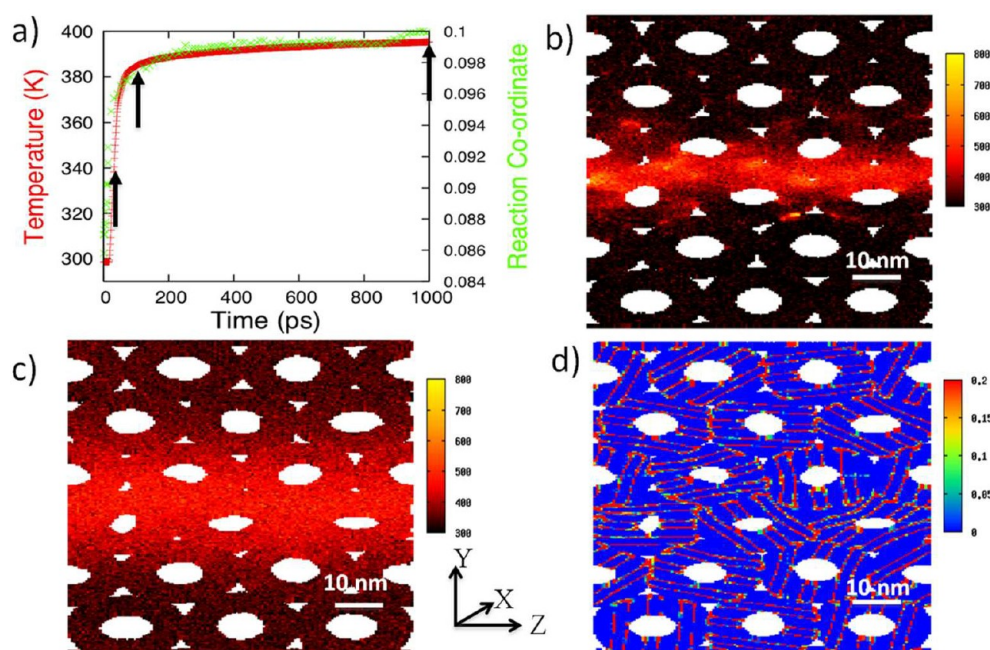
materials obtained under  $t_{\text{DM}}(4 \text{ min}) + t_{\text{WG}}(10 \text{ min})$  and  $t_{\text{DM}}(17 \text{ min}) + t_{\text{WG}}(10 \text{ min})$  conditions. It can be seen that experimental data points for all peaks fit a linear approximation. Apparent activation energies ( $E_a$ ) for both materials calculated from those dependencies are summarized in Table 1. It is worth noting that apparent activation energy for different reactions essentially does not depend on the high-energy ball-milling time.

Table 1. Apparent Activation Energies Calculated by Kissinger Method

	activation energy ( $E_a$ ), kJ/mol		
	reaction 1 (peak A)	reaction 2 (peak B)	reaction 3 (peak C)
coarse structure $t_{\text{DM}}(4 \text{ min}) + t_{\text{WG}}(10 \text{ min})$	$99 \pm 4$	$138 \pm 13$	$120 \pm 37$
nanolaminated structure $t_{\text{DM}}(17 \text{ min}) + t_{\text{WG}}(10 \text{ min})$	$93 \pm 2.5$	$145 \pm 13$	$146 \pm 14$

**3.3. Molecular Dynamics Simulations.** To understand better the molecular origin of the surprisingly low impact threshold observed experimentally, MD simulations were performed as described in Section 2.4 for a modeled system. Figure 16a shows the average temperature of the samples as a function of time for a shock with a particle velocity of 250 m/s. This velocity, higher than the threshold in the experiments, was chosen because it leads to input kinetic energy normalized by the sample mass comparable to the experimental threshold value (31.25 J/g for the simulation and 37 J/g experimentally). The shockwave runs throughout the sample in  $\sim 12.75 \text{ ps}$ , leading to a shock velocity of 4.9 km/s (nm/ps). The shock loading leads to a sharp increase in temperature (see Figure 16a) to  $\sim 345 \text{ K}$  when the shock propagates through the sample. At this time, there are large variations in local temperatures and significant internal waves in the system originating from acoustic mismatch between Ni and Al as well as solid–vacuum interfaces. The damping of these internal waves leads to an additional temperature increase (almost as much as what was caused directly by the shockwave) for  $\sim 100 \text{ ps}$ . Additional heating occurs as a result of slow chemical reactions induced by the initial heating and plastic deformation. Whereas MD time scales do not allow us to follow the reaction of the sample to completion except at extremely high impact





**Figure 16.** Time and reaction coordinate evolution of the average temperature during an MD simulation of shock loading at 250 m/s (a), local temperature maps for the dynamically loaded samples at 13.5 and 111.5 ps (b,c), and local reaction coordinate map at 1001.5 ps (d).

velocities, our simulations provide basic insight into the mechanisms of initiation and propagation.

Figure 16b,c represents local temperature maps of the system at two times after the initiation of the shockwave. At time 111.5 ps, we observe significant overheating in the regions near the impact plane and concentrated in regions near pores where significant plastic deformation has occurred. We also observe accelerated chemistry along the surfaces of the pores, where the presence of free surfaces allows higher rates of interdiffusion than in the bulk. Figure 16a, right axis, shows the evolution of the average reaction coordinate of the entire sample over time. Akin to the temperature evolution, we observe a sharp increase in the reaction variable during the passage of the shock wave, which is followed by slower reaction rates, aided by the high temperatures and plastic deformation around the pores. Figure 16d shows a map of the local reaction coordinate at time 1001.5 ps, showing the greater extent of intermixing around the pores and along the Ni/Al interfaces. We note that porosity leads to significant local heating due to local plastic deformation and mechanical intermixing even at the impact velocities studied here, where the pores do not collapse. After  $\sim 1$  ns, the temperature is rather uniform throughout the sample, but enough energy has been deposited for the chemical reaction to continue. The higher temperatures in the vicinity of the pores speed up the interdiffusion process that, in turn, generates more heat, setting off reactions that can ultimately lead to a self-propagating front. The slope of the temperature increase observed in the MD simulations indicates that temperatures of 500 K would be achieved within 10 ns (assuming that the rate of increase observed from 775 and 975 ps in the simulations remains constant) and 700 K would be reached in 20 ns. The thermal ignition measurements in Section 3.2 indicate that those values are enough for rapid chemical reactions. Therefore, the MD simulation with no tunable parameters (other than the choice of nanostructure and interatomic potential) leads to results consistent with the experimental observation and helps explain the high sensitivity of the ball-milled materials.

#### 4. DISCUSSION

This work has led to several discoveries that have allowed direct correlation between the microstructure of the high-energy ball-milled Ni+Al composite particles and their reactivity, which are discussed below.

**4.1. Ball-Milling-Induced Microstructures.** First let us consider the two types of reaction mechanisms for the formation of AlNi-based intermetallic phases through high-energy ball milling: one is a gradual reaction through elemental diffusion,<sup>33</sup> and the other is through rapid exothermic reaction initiated after a certain time of mechanical treatment.<sup>43,44</sup> Depending on experiment conditions (milling energy, ball-to-powder ratio, time, etc.) one of those mechanisms may dominate. Mild milling conditions, that is, relatively low rotation speed and ball/powder ratio, favor gradual reaction, whereas harsh milling conditions (high milling energy) generally induce the exothermic reaction. From the standpoint of exploring the reactivity and sensitivity of the system, the composites should be “activated” enough to ignite the reaction at the desired temperatures and at relatively low-energy mechanical impact; however, one should avoid gradual reactions during the ball-milling process. For this reason, a short-term combinational milling approach consisting of intensive DM up to an optimized time, followed by WG was developed and used in this work.

It was shown that under the investigated conditions of intensive high-energy ball milling the critical DM time, at which reaction ignites in the jar, is 17.5 min. In initial stages of DM the slightly deformed Ni particles cold-welded with Al phase, forming large composite agglomerations. However, further milling continuously changes the internal microstructure of such composite media. At some point, fine nanolaminated microstructure, consisting of thin Ni and Al layers, starts to form and grows on the surfaces of the large composite particles. To study the reactivity and sensitivity of two different microstructures, we employed a subsequent WG step. Such mechanical treatment using a process controlling agent enabled



further microstructural refinement of the composite particles without triggering the exothermic reaction. The fragmentation of primary cold-welded composite particles resulted in the formation of fine particles with a larger portion of fine nanolaminated microstructure. Changing the DM time and the addition of wet processing also allowed control of the microstructure of ball-milled materials (Figure 6) without undesired changes in phase composition and led to materials with tailored reactivity and sensitivity as a function of DM time.

**4.2. Reactivity and Sensitivity of Ni+Al Composite Particles.** As was already outlined in the Introduction, high-energy ball milling significantly decreases the ignition temperature in Ni+Al system.<sup>1,9,13,14,17</sup> An important result of this work is that a direct correlation was found between the ignition characteristics and specific microstructure of the composite particles. Indeed it was demonstrated that two distinct milling-induced microstructures (Figure 5) show different ignition characteristics. The material with predominantly fine nanolaminated structure can be ignited at very low temperatures ( $\sim 500$  K). The ignition temperature for coarse microstructure is significantly higher ( $\sim 700$  K). It is worth noting that the ignition temperature, observed in current work for the particles prepared under optimized ball-milling conditions, is the lowest reported in literature.

Similar to thermal ignition, previous reports<sup>1,17,18</sup> showed that ball milling significantly decreases the value of the critical energy of mechanical impact that requires us to initiate reaction in Ni+Al system. The value of  $\sim 100$  J found in this work is the lowest reported to date when compared to the previous data, 420 J.<sup>17</sup> Impact initiation experiments showed that under the same conditions (e.g.,  $F_2$  fraction, 72% TMD,  $W = 210$  J) samples compacted from the powder with coarse microstructure could not be ignited, whereas samples with a large portion of nanolaminated structure were ignited consistently. Another interesting result, which is contrary to the thermal initiation, is that the particle size of composites does not affect the threshold on the reaction initiation by mechanical impact, as long as the fine microstructure is dominant. An important question to answer is whether there is a direct correlation between low thermal ignition temperature and the low critical energy of mechanical impact.

High-speed imaging revealed that after impact hot spots appear at the plunger interface with 1–32 ms delay. (See, for example, Figure 9.) Then, a reaction wave starts to propagate throughout the sample with a velocity of  $\sim 20$  cm/s. Additional experiments showed that the reaction front for a similar sample ignited by thermal source, under the same heat loss conditions, also propagates with combustion velocity of  $\sim 20$  cm/s. The results of MD simulations showed (Figure 16) that the formation of hot spots can be due to the collapse of natural porosity within the sample. Following the passage of the shock wave, the local temperature may increase in two ways. First, plastic deformation increases the temperature in the material surrounding the pore. In the second way, during the pore collapsing, Ni and Al atoms flow along the free surfaces of the pores, and as a result, intermixing is faster than that in the bulk.<sup>29</sup> The combined effect of these two processes can raise the temperature in the vicinity of the pores by as much as 600 K for an impact velocity of 250 m/s. The main conclusion from these results is that under the investigated conditions the impact initiation of reaction has a thermal nature; that is, the peak temperature at hot spots is on the same order as that for the thermal ignition temperature case.

**4.3. Reaction Mechanism.** Finally, let us consider the issue of reaction mechanism in Ni+Al composite particles initiated by mechanical impact. Our results confirm that solid-state reactions are responsible for the observed ignition processes. Analysis of microstructure for reacted materials shows that particles kept their shape and morphology after reaction (Figure 13), which may indicate that the process proceeds under essentially solid-state conditions. Calculated heat of reaction from DSC experiments also indicates that for composite particles conversion mainly takes place below eutectic (912 K), whereas for conventional mixture of Ni and Al powders the reaction begins above this temperature.<sup>14</sup>

Comparing DSC curves with impact initiation experiments and XRD results of quenched materials allows us to conclude that the reaction initiation at low temperatures corresponds to nickel dissolution in aluminum (peak A, Figure 12). However, the main heat release occurs in the next two stages where formation of intermetallic phases takes place. Analysis of DSC curves also indicates that for material with the coarse microstructure the exothermic solid-state dissolution of nickel at aluminum lattice proceeds, but it is with slower rate as compared with material that has the nanolaminated structure. Therefore, it can be inferred that such differences make nanolaminated material more sensitive, and the reaction can be initiated at unusually low temperatures ( $\sim 500$  K).

Previous research showed that ball milling reduced the apparent activation energy ( $E_a$ ) of the Ni-clad-Al system from  $351 \pm 8$  to  $117 \pm 4$  kJ/mol.<sup>14</sup> Electrothermal explosion investigation<sup>13</sup> provided  $E_a$  values of  $104 \pm 8$  kJ/mol, which is close to the value obtained in present research for solid-state dissolution of nickel in aluminum. It is more important that obtained kinetic parameters (Table 1) suggest that the milling time and microstructure of the material has little influence on the apparent activation energies of the process. These results can be explained if one assumes that the energy barrier for nickel diffusion to aluminum is significantly changed when the media transforms from the initial mixture with point contacts between the metal particles to the composite pore free media with fresh metal/metal boundaries (see ref 24), whereas further mechanical treatment does not influence much the value of this energy barrier. In the current work, it was shown that after 4 min of ball milling, when a composite structure forms, further milling does not influence the apparent activation energy. However, further milling does greatly increase the contact between reagents and by this enhances the overall kinetics. As long as  $E_a$  for solid-state dissolution of nickel in aluminum lattice is the same for both materials, the dominant factor becomes the contact surface area. Nanolaminated structure has greater contact between reactants, and nickel more readily dissolves in the aluminum lattice. The latter makes nanolaminated structure more reactive and sensitive.

## 5. FINAL REMARKS

This work has clearly shown that by utilizing a combined milling approach reactive composite particles with tailored reactivity can be obtained. The low thermal ignition and mechanical impact ignition thresholds are a result of the milling-induced nanolaminated microstructure and, depending on the fraction present within the composite particle, may be as low as  $\sim 500$  K and 100 J respectively. As previously discussed, this work has answered some fundamental questions related to the reactive nature of composite materials produced by high-energy ball milling. However, several issues still remain, which

are presently being addressed. The first is whether the initiation mechanism under high-energy impact (10–100 kJ) remains the same as that for the case of low-energy (100 J) mechanical impact investigated in this work. Shear-impact experiments allow in situ observation of the reaction process under both low- and high-impact energy conditions, which allows investigation of such processes. Second, concerning the reaction mechanism for the nanocomposite materials formed by ball milling, can one apply the conclusions made for Ni+Al system to other high-energy density systems such as Ti+C, Ta+C, Ti+B, and so on? The answer is not obvious, and additional studies are required to address this question. Whereas application of MD simulation in this work was helpful for the explanation of the observed results on the impact initiation of the reaction in Ni+Al system, a predictive multiscale theoretical framework that predicts the performance of nanostructured reactive materials with chemistry and nanostructure as the only inputs remains elusive due to the disparate scales that govern the performance of these materials. Finally, another promising area for further investigation is related to the properties of the products formed under different conditions, that is, thermal ignition and low- and high-energy shock wave initiation, which may lead to the synthesis of novel advanced materials.

## AUTHOR INFORMATION

### Corresponding Author

\*Phone: 574-631-5796. Fax: 574-631-8366. E-mail: kmanukya@nd.edu.

### Notes

The authors declare no competing financial interest.

## ACKNOWLEDGMENTS

Funding from the Defense Threat Reduction Agency (DTRA), Grant Number HDTRA1-10-1-0119. Counter-WMD basic research program, Dr. Suhithi M. Peiris, program director is gratefully acknowledged. Khachatur Manukyan also thanks Fulbright Program from the Bureau of Educational and Cultural Affairs of the U.S. Department of State. We thank Prof. Alberto Cuitino (Rutgers, The State University of New Jersey) for fruitful discussion and Prof. Paul J. McGinn (University of Notre Dame) for assistance in XRD measurements. This work was also partially supported by Notre Dame Integrated Imaging Facility (NDIIF).

## REFERENCES

- (1) Reeves, R. V.; Mukasyan, A. S.; Son, S. F. *J. Phys. Chem. C* **2010**, *114*, 14772–14780.
- (2) Mukasyan, A. S.; Rogachev, A. S. *Prog. Energy Combust. Sci.* **2008**, *34*, 377–416.
- (3) Biswas, A.; Roy, S. K. *Acta Mater.* **2004**, *52*, 257–270.
- (4) Morsi, K. *Mater. Sci. Eng., A* **2001**, *299*, 1–15.
- (5) Fritz, G. M.; Joress, H.; Weihs, T. P. *Combust. Flame* **2011**, *158*, 1084–1088.
- (6) Tappan, B. C.; Huynh, M. H.; Hiskey, M. A.; Chavez, D. E.; Luther, E. P.; Mang, J. T.; Son, S. F. *J. Am. Chem. Soc.* **2006**, *128*, 6589–6594.
- (7) Bockmon, B. S.; Pantoya, M. L.; Son, S. F.; Asay, B. W.; Mang, J. T. *J. Appl. Phys.* **2005**, *98*, 64903-1–64903-7.
- (8) Athanassiou, E. K.; Grass, R. N.; Osterwalder, N.; Stark, W. J. *Chem. Mater.* **2007**, *19*, 4847–4854.
- (9) Shoshin, Y. L.; Mudryy, R. S.; Dreizin, E. L. *Combust. Flame* **2002**, *128*, 259–269.
- (10) Hunt, E. M.; Pantoya, M. L. *Intermetallics* **2010**, *18*, 1612–1616.
- (11) Filimonov, V. Y.; Korchagin, M. A.; Smirnov, E. V.; Sytnikov, A. A.; Yakovlev, V. I.; Lyakhov, N. Z. *Intermetallics* **2011**, *19*, 833–840.
- (12) Crone, J. C.; Knap, J.; Chung, P. W.; Rice, B. M. *Appl. Phys. Lett.* **2011**, *98*, 141910-1–141910-3.
- (13) Shteinberg, A. S.; Lin, Y. -C.; Son, S. F.; Mukasyan, A. S. *J. Phys. Chem. A* **2010**, *114*, 6111–6116.
- (14) White, J. D. E.; Reeves, R. V.; Son, S. F.; Mukasyan, A. S. *J. Phys. Chem. A* **2009**, *113*, 13541–13547.
- (15) Hadjiafxenti, A.; Gunduz, I. E.; Tsotsos, C.; Kyratsi, T.; Doumanidis, C. C.; Rebholz, C. *Intermetallics* **2010**, *18*, 2219–2223.
- (16) Moore, J. J.; Feng, H. *J. Prog. Mater. Sci.* **1995**, *39*, 243–273.
- (17) Herbold, E. B.; Thadhani, N. N.; Jordan, J. L. *J. Appl. Phys.* **2011**, *109*, 066108-1–066108-3.
- (18) Eakins, D. E.; Thadhani, N. N. *Int. Mater. Rev.* **2009**, *54*, 181–213.
- (19) Song, I.; Thadhani, N. N. *Metall. Mater. Trans. A* **1992**, *23*, 41–48.
- (20) Semenov, N. N. *Z. Phys.* **1928**, *48*, 571–582.
- (21) Rice, O. K.; Allen, A. O.; Campbell, H. C. *J. Am. Chem. Soc.* **1935**, *57*, 2212–2222.
- (22) Frank-Kamenetskii, D. A. *Diffusion and Heat Exchange in Chemical Kinetics*; Princeton University Press: Princeton, NJ, 1955.
- (23) Merzhanov, A. G. *Combust. Flame* **1966**, *10*, 341–348.
- (24) Mukasyan, A. S.; Khina, B. B.; Reeves, R. V.; Son, S. F. *Chem. Eng. J.* **2011**, *174*, 677–686.
- (25) Thiers, L.; Mukasyan, A. S.; Varma, A. *Combust. Flame* **2002**, *131*, 198–209.
- (26) Zhu, P.; Li, J. C. M.; Liu, C. T. *Mater. Sci. Eng., A* **2002**, *329*–331, 57–68.
- (27) Weingarten, N. S.; Mattson, W. D.; Yau, A. D.; Weihs, T. P.; Rice, B. M. *J. Appl. Phys.* **2010**, *107*, 093517-1–093517-10.
- (28) Weingarten, N. S.; Rice, B. M. *J. Phys.: Condens. Matter* **2011**, *23*, 275701-1–275701-9.
- (29) Cherukara, M. J.; Karthik, G. V.; Strachan, A. *Phys. Rev. B* **2012**, under review.
- (30) Suryanarayana, C. *Prog. Mater. Sci.* **2001**, *46*, 1–184.
- (31) Takacs, L. *Prog. Mater. Sci.* **2002**, *47*, 355–414.
- (32) Gaffet, E.; Bernard, F.; Niepce, J. -C.; Charlot, F.; Gras, C.; Caer, G.; Guichard, J. -L.; Delcroix, P.; Mocellinc, A.; Tillement, O. *J. Mater. Chem.* **1999**, *9*, 305–314.
- (33) Moshksar, M. M.; Mirzaee, M. *Intermetallics* **2004**, *12*, 1361–1366.
- (34) Asay, B. W.; Henson, B. F.; Dickson, P. M.; Fugard, C. S.; Funk, D. J. *AIP Conf. Proc.* **1998**, *429*, 567–570.
- (35) Kissinger, H. E. *Anal. Chem.* **1957**, *29*, 1702–1706.
- (36) Plimpton, S. J. LAMMPS Code. <http://lammps.sandia.gov>.
- (37) Plimpton, S. J. *J. Comput. Phys.* **1995**, *117*, 1–19.
- (38) Purja, G. P.; Mishin, Y. *Philos. Mag.* **2009**, *89*, 3245–3267.
- (39) Zhao, S.; Germann, T.; Strachan, A. *Phys. Rev. B* **2007**, *76*, 014103-1–014103-6.
- (40) Zhao, S.; Germann, T.; Strachan, A. *Phys. Rev. B* **2007**, *76*, 014105-1–014105-5.
- (41) Zhao, S.; Germann, T.; Strachan, A. *J. Chem. Phys.* **2006**, *125*, 164707-1–164707-8.
- (42) Collins, T. J. *BioTechniques* **2007**, *43*, 25–30.
- (43) Pabi, S. K.; Murty, B. S. *Mater. Sci. Eng., A* **1996**, *214*, 146–152.
- (44) Atzmon, M. *Phys. Rev. Lett.* **1990**, *64*, 487–490.
- (45) Holian, B. L. *Phys. Rev. A* **1988**, *37*, 2562.